

# Dark-Field Tomography of an Attenuating Object Using Intrinsic X-Ray Speckle-Tracking

S. J. Alloo<sup>a</sup>, D. M. Paganin<sup>b</sup>, K. S. Morgan<sup>b</sup>, M. J. Kitchen<sup>b</sup>, A. W. Stevenson<sup>c</sup>, S. C. Mayo<sup>d</sup>,  
H. T. Li<sup>e</sup>, B. M. Kennedy<sup>f</sup>, A. Maksimenko<sup>c</sup>, J. Bowden<sup>d</sup>, and K. M. Pavlov<sup>a, b, g</sup>

<sup>a</sup>School of Physical and Chemical Sciences, University of Canterbury, Christchurch, 8041, New Zealand

<sup>b</sup>School of Physics and Astronomy, Monash University, Victoria 3800, Australia

<sup>c</sup>Australian Synchrotron, ANSTO, Clayton, Victoria 3168, Australia

<sup>d</sup>Commonwealth Scientific and Industrial Research Organisation, Clayton, Victoria 3168, Australia

<sup>e</sup>School of Mathematics, University of Canterbury, Christchurch, 8041, New Zealand

<sup>f</sup>School of Earth and Environment, University of Canterbury, Christchurch, 8041, New Zealand

<sup>g</sup>University of New England, Armidale, New South Wales 2351, Australia

## ABSTRACT

**Purpose:** To investigate how an intrinsic speckle-tracking approach to speckle-based X-ray imaging can be used to extract an object's effective dark-field signal, which is capable of providing object information in three dimensions.

**Approach:** The effective dark-field signal was extracted using a Fokker-Planck type formalism, which models the deformations of illuminating reference-beam speckles due to both coherent and diffusive scatter from the sample. We here assumed that (a) small-angle scattering fans at the exit surface of the sample are rotationally symmetric, and (b) the object has both attenuating and refractive properties. The associated inverse problem, of extracting the effective dark-field signal, was numerically stabilised using a "weighted determinants" approach.

**Results:** Effective dark-field projection images are presented, as well as the dark-field tomographic reconstructions of the wood sample. Dark-field tomography was performed using a filtered-back projection reconstruction algorithm. The dark-field tomographic reconstructions of the wood sample provided complementary, and otherwise inaccessible, information to augment the phase-contrast reconstructions, which were also computed.

**Conclusions:** An intrinsic speckle-tracking approach to speckle-based imaging can tomographically reconstruct an object's dark-field signal at a low sample exposure and with a simple experimental set-up. The obtained dark-field reconstructions have image quality comparable to alternative X-ray dark-field techniques.

**Keywords:** Dark Field Computed Tomography, Speckle X-ray Imaging, Intrinsic Speckle Tracking

## 1. INTRODUCTION

X-rays have been utilized in a variety of applications since their discovery by Röntgen.<sup>1</sup> Their ability to pass through matter makes X-rays highly useful in a broad range of applications, particularly in medical imaging. X-rays are attenuated, scattered, and refracted when traversing a material. As a result, the wavefield at the exit surface of the object contains encoded information regarding that object. X-ray imaging directly visualises differing densities, and therefore refractive indices, of materials within a sample. The refractive index for X-rays

---

Further author information: (Send correspondence to S. J. Alloo)  
S. J. Alloo: samantha.alloo@pg.canterbury.ac.nz,  
K. M. Pavlov: konstantin.pavlov@canterbury.ac.nz

travelling through matter is given as  $n(\mathbf{r}') = 1 - \delta(\mathbf{r}') + i\beta(\mathbf{r}')$ , where  $\mathbf{r}'$  is the three-dimensional position vector, and  $\delta(\mathbf{r}')$  and  $\beta(\mathbf{r}')$  describe refraction and attenuation of the X-ray beam, respectively. In many X-ray imaging techniques, it is these functions that provide the relative image contrast, for example conventional radiography is attenuation-based imaging, and hence depends on  $\beta(\mathbf{r}')$ .

Phase-contrast imaging (PCI)<sup>2</sup> is an X-ray imaging technique that exploits the refraction of X-rays in material. PCI is especially useful for imaging objects that are weakly attenuating, e.g. soft tissues in mammography. Propagation-based phase-contrast imaging (PB-PCI)<sup>3-6</sup> is a PCI technique that achieves phase-contrast by making use of sufficiently spatially-coherent illumination and subsequent downstream free-space propagation of the exit-surface wavefront. PB-PCI is a refraction- and attenuation-based radiography technique, which is easily-implemented, as no additional optical elements are required. PB-PCI can be used to non-invasively study samples at micrometre and sub-micrometre length scales. The downstream propagation in PB-PCI allows the extraction of phase information, relating to  $\delta(\mathbf{r}')$ , via suitable phase-retrieval algorithms. This phase information is lost in attenuation-based X-ray imaging techniques. Paganin *et al.*<sup>7</sup> demonstrated a simple phase-retrieval algorithm for a single-material object using PB-PCI, which is based on the transport-of-intensity equation.<sup>8</sup>

Some methods achieve phase-contrast by introducing additional optical elements, for example, grating interferometry,<sup>9-14</sup> single-grid PCI,<sup>15</sup> Bonse-Hart interferometry,<sup>16-18</sup> edge-illumination PCI,<sup>19,20</sup> and analyser-based PCI.<sup>21-25</sup> Speckle-based X-ray imaging (SBXI), first introduced in 2012 by Berujon *et al.*<sup>26</sup> and Morgan *et al.*,<sup>27</sup> uses a spatially random mask placed between the X-ray source and detector (see Fig. 1). This mask acts as a random phase and intensity modulator to generate a near-field speckle pattern. In this technique, information regarding the sample is inferred by studying how the speckles, first measured in the absence of the object, are altered by the introduction of the object. Using such an approach, SBXI is capable of reconstructing phase gradients, attenuation, and small-angle scattering information.<sup>28</sup>

Spatial resolution in PCI is limited by the size of the detector pixels and the size of the x-ray source. As a result, micro-structure smaller than the resolution of the imaging system, and hence smaller than the pixel size, cannot be imaged directly. Dark-field (DF) X-ray imaging provides information about such spatially-unresolved microstructure. DF thereby enables complementary structural information to be obtained at sub-pixel scales. Image contrast in DF imaging is generated by position-dependent small-angle X-ray scattering (SAXS) of the incident beam by the sample. SAXS<sup>29</sup> is the diffusive scattering of an X-ray beam from unresolved microstructures that are smaller than the width of a pixel, and are found within an object. This position-dependent SAXS influences the measured PCI data, leading to the associated inverse problem<sup>30</sup> of how information regarding the spatially-unresolved microstructure (e.g. a position-dependent correlation length) may be inferred from one or more measured PCI images.

Currently, there are a variety of DF-PCI techniques, e.g. propagation-based DF-PCI,<sup>31,32</sup> grating-based DF-PCI,<sup>33-36</sup> edge-illumination DF-PCI,<sup>37,38</sup> and analyzer-based DF-PCI.<sup>25,39-42</sup> Grating-based PCI has regular gratings placed between the source and detector, for example, the so-called Talbot-Lau interferometer reported by David *et al.* and Momose *et al.*<sup>9,10</sup> In such techniques, the attenuation, differential phase and DF signal can be extracted by measuring the intensity variations caused by introducing the sample in the path of the beam. However, to do so, several different image acquisitions are required to reconstruct a single projection. This is done using different transverse positions of the gratings, relative to one another. Single-grating-based methods have also been reported,<sup>43,44</sup> aiming to reduce the X-ray exposure relative to multi-grating-based approaches. Analyzer-based imaging, similarly to grating-based imaging, requires multiple image acquisitions to reconstruct a single projection of the object. In this technique, an analyzer crystal is introduced to selectively measure angular components of the X-ray beam. Kitchen *et al.*<sup>45-47</sup> and Ando *et al.*<sup>41</sup> used a Laue geometry, to simultaneously collect transmitted and diffracted images, to reconstruct both the absorption and phase images in a single exposure. As a result, both the exposure time and radiation dose were considerably reduced compared to alternative techniques that rotate the analyzer crystal.

SBXI techniques are also capable of extracting DF images, through speckle tracking.<sup>48-51</sup> Berujon and Ziegler<sup>51</sup>

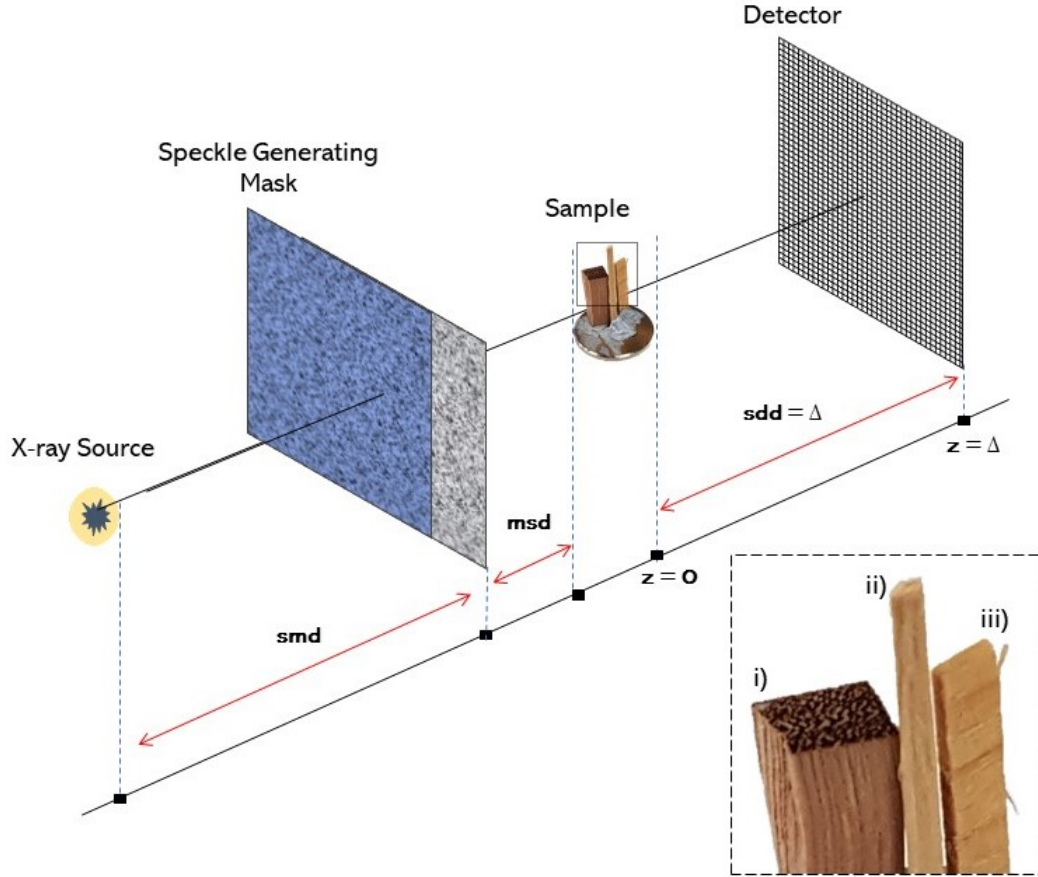


Figure 1. Schematic of Speckle-Based X-ray Imaging (SBXI) experimental setup. Here,  $smd$  is the source-to-mask distance,  $msd$  is the mask-to-sample distance, and  $sdd = \Delta$  is the sample-to-detector distance.

92 use “X-ray Speckle-Vector Tracking” (XSVT), and Zdora *et al.*<sup>49</sup> employ the formalism of “Unified Modu-  
 93 lated Pattern Analysis” (UMPA). XSVT and UMPA alike apply an explicit, pixel-wise tracking approach to  
 94 extract the DF signal by analysing multiple SBXI images. However, single-image multimodal recovery is also  
 95 possible using a correlation based approach.<sup>27,50</sup> Pavlov *et al.* recently developed “Multimodal Intrinsic Speckle-  
 96 Tracking” (MIST)<sup>52,53</sup>, an algorithm able to retrieve a sample’s DF signal in SBXI. MIST<sup>52</sup> utilizes intrinsic  
 97 speckle-tracking within a SBXI set-up to recover an object’s phase and DF signal simultaneously, in a determin-  
 98 istic manner. MIST combines a Fokker-Planck<sup>31,54,55</sup> description of paraxial X-ray optics with a geometric-flow  
 99 formalism for X-ray speckle tracking.<sup>56</sup> The MIST<sup>52</sup> formalism only requires two sets of projection data, for two  
 100 different transverse positions of the mask, suggesting that the technique may be suitable for clinical applications  
 101 where dose should be minimised. DF images have proven highly advantageous in the study of soft tissues,<sup>57</sup> and  
 102 the success of SBXI techniques in PCI has also been highlighted.<sup>58</sup>

103  
 104 The speckle-tracking variant of obtaining the DF signal published by Pavlov *et al.*<sup>52</sup> assumes that (a) the  
 105 sample is non-attenuating, and (b) the position-dependent SAXS fans that emanate from the exit surface of  
 106 the object are rotationally symmetric. Here, we extend the MIST formalism<sup>52</sup> to consider a monomorphous at-  
 107 tenuating object, while maintaining the assumption of rotationally-symmetric SAXS fans. Such generalizations  
 108 are crucial for the broader utility of this technique—e.g. in possible future applications to disciplines such as  
 109 metallurgy, paleontology, soils science and structural failure prediction—since typical samples in such contexts  
 110 are often strongly attenuating.

111

## 2. THEORY

112

113 Here we extend the MIST<sup>52</sup> formalism to the case of a monomorphous attenuating object, by first formulating  
 114 the forward problem and then solving the corresponding inverse problem.<sup>30</sup> The forward-finite-difference Fokker-  
 115 Planck equation is first obtained, which can be used to model optical energy conservation as the speckles are  
 116 formed and then deformed due to propagation through a SAXS-inducing object. The inverse problem for a  
 117 monomorphous attenuating object is then considered, aiming to retrieve both (a) the effective-DF signal and (b)  
 118 projected thickness (which can be related to the object-induced phase shifts). We also consider two approaches  
 119 to numerically stabilise the mildly-ill-posed inverse problem.

### 120 2.1 Scalar-Diffusion Fokker-Planck Formalism for X-ray Speckle-Tracking: 121 Monomorphous Attenuating Object Approximation

122 We begin by assuming that a monomorphous attenuating object is placed in a spatially-well-resolved reference  
 123 speckle field, as in Fig. 1. The reference speckle field, together with the corresponding images in the presence of  
 124 the sample, obey the Fokker-Planck<sup>55</sup> generalisation<sup>31,54</sup> of the geometric flow formalism<sup>56</sup> for speckle-tracking.  
 125 Now, following Pavlov *et al.*,<sup>52</sup> and Paganin and Morgan,<sup>31,54</sup> we have the Fokker-Planck equation for SBXI,  
 126 which models coherent flow and diffusive flow for a phase object described by its phase shift,  $\phi_{\text{ob}}(\mathbf{r})$ , and effective  
 127 scalar diffusion coefficient,  $D_{\text{eff, Phase}}(\mathbf{r}; \Delta)$ , as:

$$I_R(\mathbf{r}) - I_S(\mathbf{r}) = \frac{\Delta}{k} \nabla_{\perp} \cdot [I_R(\mathbf{r}) \nabla_{\perp} \phi_{\text{ob}}(\mathbf{r})] - \Delta \nabla_{\perp}^2 [D_{\text{eff, Phase}}(\mathbf{r}; \Delta) I_R(\mathbf{r})]. \quad (1)$$

128

129 This expression relates the reference speckle image intensity,  $I_R(\mathbf{r})$ , obtained with no sample in the beam, to the  
 130 encoded form of the speckle image,  $I_S(\mathbf{r})$ , which is obtained in the presence of the sample. Here,  $(\mathbf{r}) \equiv (x, y)$   
 131 denote Cartesian coordinates in planes perpendicular to the optical axis  $z$ ,  $\Delta$  is the sample-to-detector distance,  
 132  $k$  is the wavenumber of the X-rays,  $\nabla_{\perp} = (\partial/\partial x, \partial/\partial y)$  is the gradient operator in the  $(x, y)$  plane, and  $\nabla_{\perp}^2$  is  
 133 the transverse Laplacian operator.

134

135 Next, we consider Eqn. (9) from Pavlov *et al.*,<sup>58</sup> which gives the variation in registered intensity of a well  
 136 resolved speckle field due to an attenuating object as:

$$\frac{I_S}{I_R} \approx I_{\text{ob}}(\mathbf{r}) - \frac{\Delta}{k} \nabla_{\perp} \cdot [I_{\text{ob}}(\mathbf{r}) \nabla_{\perp} \phi_{\text{ob}}(\mathbf{r})]. \quad (2)$$

137

138 Here,  $I_{\text{ob}}(\mathbf{r})$  describes the intensity at the exit surface of the sample,  $z = 0$ , after the object has attenuated the  
 139 incident X-ray beam of unit intensity. It should be noted that the above expression only models the coherent  
 140 flow of X-rays through the sample. We can now combine this with the Fokker-Planck equation for a phase object,  
 141 Eqn. (1), to give the Fokker-Planck equation for an attenuating object as:

$$I_R(\mathbf{r}) I_{\text{ob}}(\mathbf{r}) - I_S(\mathbf{r}) = \frac{\Delta}{k} \nabla_{\perp} \cdot [I_R(\mathbf{r}) I_{\text{ob}}(\mathbf{r}) \nabla_{\perp} \phi_{\text{ob}}(\mathbf{r})] - \Delta \nabla_{\perp}^2 [D_{\text{eff, Atten}}(\mathbf{r}; \Delta) I_R(\mathbf{r}) I_{\text{ob}}(\mathbf{r})]. \quad (3)$$

142 This forward-finite-difference continuity equation is formulated on the basis of local energy conservation within  
 143 the system. The first term on the right-hand side describes coherent energy flow, with the second describing the  
 144 diffusive component. The coherent term models local absorption, lensing and prism-like effects,<sup>31</sup> which are also  
 145 seen in the transport-of-intensity equation.<sup>8</sup> The diffusion term describes the position-dependent local blurring  
 146 which is associated with the SAXS fans at the exit surface of the object. Here, we remind the reader that the  
 147 position-dependent SAXS fans are approximated as rotationally symmetric.

148

149 We now assume that the effective DF signal,  $D_{\text{eff, Atten}}(\mathbf{r}; \Delta)$ , is a slowly varying function of the transverse  
 150 positions, so that it approximately commutes with the transverse Laplacian operator. Moreover, we can neglect  
 151 the transverse spatial derivatives of  $D_{\text{eff, Atten}}(\mathbf{r}; \Delta)$  as they will be small compared to the retained terms. Several  
 152 components arise when the second derivative of the second term in Eqn. (3) is evaluated. Many of these can be  
 153 neglected, using an approximation employed by Pavlov *et al.*<sup>52,58</sup>: an average, of the scalar product of a rapidly

154 varying vector field with a more slowly changing gradient of the product of two functions, can be neglected. Then,

$$155 \frac{I_S(\mathbf{r})}{I_R(\mathbf{r})} = I_{\text{ob}}(\mathbf{r}) - \frac{\Delta}{k} \nabla_{\perp} \cdot [I_{\text{ob}}(\mathbf{r}) \nabla_{\perp} \phi_{\text{ob}}(\mathbf{r})] + \frac{\Delta D_{\text{eff, Atten}}(\mathbf{r}; \Delta) I_{\text{ob}}(\mathbf{r}) \nabla_{\perp}^2 I_R(\mathbf{r})}{I_R(\mathbf{r})} + \Delta D_{\text{eff, Atten}}(\mathbf{r}; \Delta) \nabla_{\perp}^2 I_{\text{ob}}(\mathbf{r}). \quad (4)$$

156 We proceed by using the projection approximation for a single-material object,<sup>59</sup>

$$157 \phi_{\text{ob}}(\mathbf{r}) = -k\delta t(\mathbf{r}), \quad (5)$$

$$158 I_{\text{ob}}(\mathbf{r}) = e^{-2k\beta t(\mathbf{r})} = e^{-\mu t(\mathbf{r})}, \quad (6)$$

159 where  $\mu = 2k\beta$  is the linear attenuation coefficient of the single-material object, and  $t(\mathbf{r})$  is the projected thickness  
160 of the object along the direction of the X-rays, to give:

$$161 \frac{I_S(\mathbf{r})}{I_R(\mathbf{r})} = \left(1 - \frac{\gamma\Delta}{2k} \nabla_{\perp}^2\right) I_{\text{ob}}(\mathbf{r}) + \frac{\Delta D_{\text{eff, Atten}}(\mathbf{r}; \Delta) I_{\text{ob}}(\mathbf{r}) \nabla_{\perp}^2 I_R(\mathbf{r})}{I_R(\mathbf{r})} + \Delta D_{\text{eff, Atten}}(\mathbf{r}; \Delta) \nabla_{\perp}^2 I_{\text{ob}}(\mathbf{r}). \quad (7)$$

162 This expression models the forward-problem of encoding a given well-resolved reference speckle field by putting  
163 an attenuating object in the beam path, where  $\gamma = \delta/\beta$ .

164 We now turn to the inverse problem. Define the additional functions:

$$165 G_1(\mathbf{r}) = \left(1 - \frac{\gamma\Delta}{2k} \nabla_{\perp}^2\right) I_{\text{ob}}(\mathbf{r}) + \Delta D_{\text{eff, Atten}}(\mathbf{r}; \Delta) \nabla_{\perp}^2 I_{\text{ob}}(\mathbf{r}), \quad (8)$$

$$166 G_2(\mathbf{r}) = \Delta D_{\text{eff, Atten}}(\mathbf{r}; \Delta) I_{\text{ob}}(\mathbf{r}), \quad (9)$$

$$167 G(\mathbf{r}) = \left(1 - \frac{\gamma\Delta}{2k} \nabla_{\perp}^2\right) I_{\text{ob}}(\mathbf{r}). \quad (10)$$

168 The function  $G(\mathbf{r})$ , which describes the coherent component of the optical flow, can be written in terms of the  
169 defined functions  $G_1(\mathbf{r})$  and  $G_2(\mathbf{r})$ . That is, we apply the Laplacian operator to  $G_2(\mathbf{r})$ , once again assuming  
170  $D_{\text{eff, Atten}}(\mathbf{r}; \Delta)$  to be slowly varying, to give:

$$171 \nabla_{\perp}^2 G_2(\mathbf{r}) = \Delta D_{\text{eff, Atten}}(\mathbf{r}; \Delta) \nabla_{\perp}^2 I_{\text{ob}}(\mathbf{r}). \quad (11)$$

172 Hence,

$$173 G(\mathbf{r}) = G_1(\mathbf{r}) - \nabla_{\perp}^2 G_2(\mathbf{r}). \quad (12)$$

Equation (7) can now be expressed in terms of the defined functions  $G_1(\mathbf{r})$  and  $G_2(\mathbf{r})$ , to give:

$$174 \frac{I_S(\mathbf{r})}{I_R(\mathbf{r})} = G_1(\mathbf{r}) + \frac{G_2(\mathbf{r}) \nabla_{\perp}^2 I_R(\mathbf{r})}{I_R(\mathbf{r})}. \quad (13)$$

175 It is important to note here that the functions  $G_1(\mathbf{r})$  and  $G_2(\mathbf{r})$  are independent of the illuminating speckle field,  
176 hence they are unaffected by the transverse position of the speckle-generating mask. Hence, if two independent  
177 measurements of  $I_S(\mathbf{r})$  and  $I_R(\mathbf{r})$  are taken, e.g., by using two different positions of the mask, a system of linear  
178 equations is obtained. These linear equations can be solved for the attenuation term,  $I_{\text{ob}}(\mathbf{r})$ , and the effective  
179 DF signal,  $D_{\text{eff, Atten}}(\mathbf{r}; \Delta)$ .

180 Specifically, if  $I_{S1, S2}(\mathbf{r})$  and  $I_{R1, R2}(\mathbf{r})$  denote the sample image, and well resolved speckle image for positions 1  
181 and 2 of the mask, respectively,

$$\begin{cases} \frac{I_{S1}(\mathbf{r})}{I_{R1}(\mathbf{r})} = G_1(\mathbf{r}) + \frac{G_2(\mathbf{r}) \nabla_{\perp}^2 I_{R1}(\mathbf{r})}{I_{R1}(\mathbf{r})}, \\ \frac{I_{S2}(\mathbf{r})}{I_{R2}(\mathbf{r})} = G_1(\mathbf{r}) + \frac{G_2(\mathbf{r}) \nabla_{\perp}^2 I_{R2}(\mathbf{r})}{I_{R2}(\mathbf{r})}. \end{cases} \quad (14)$$

182 Solving these equations gives:

$$G_1(\mathbf{r}) = \frac{I_{S1}(\mathbf{r})}{I_{R1}(\mathbf{r})} - \frac{G_2(\mathbf{r})\nabla_{\perp}^2 I_{R2}(\mathbf{r})}{I_{R2}(\mathbf{r})}, \quad (15)$$

$$G_2(\mathbf{r}) = \frac{I_{R1}(\mathbf{r})I_{S2}(\mathbf{r}) - I_{R2}(\mathbf{r})I_{S1}(\mathbf{r})}{I_{R1}(\mathbf{r})\nabla_{\perp}^2 I_{R2}(\mathbf{r}) - I_{R2}(\mathbf{r})\nabla_{\perp}^2 I_{R1}(\mathbf{r})}. \quad (16)$$

183 Using the approach presented in Paganin *et al.*,<sup>7</sup> and the definition of  $G_2(\mathbf{r})$ , the effective DF signal  $D_{\text{eff, Atten}}(\mathbf{r}; \Delta)$   
 184 and projected thickness  $t(\mathbf{r})$ , of a SAXS-inducing attenuating object, are given as:

$$t(\mathbf{r}) = \frac{-1}{\mu} \log_e \mathcal{F}^{-1} \left[ \frac{\mathcal{F} G(\mathbf{r})}{1 + \gamma \Delta \lambda \pi (u^2 + v^2)} \right], \quad (17)$$

$$D_{\text{eff, Atten}}(\mathbf{r}; \Delta) = \frac{G_2(\mathbf{r})}{\Delta I_{\text{ob}}(\mathbf{r})}. \quad (18)$$

186 In Eqn. (17),  $\mathcal{F}$  denotes Fourier transformation with respect to  $x$  and  $y$ , for which the corresponding Fourier-  
 187 space variables are  $u$  and  $v$ , respectively, and  $\lambda$  is the X-ray wavelength. It should be highlighted that the  
 188 expression for the effective DF of an attenuating object, namely Eqn. (18) above, is equivalent to Eqn. (7) from  
 189 Pavlov *et al.*,<sup>52</sup> for the special case of a phase object.

## 190 2.2 Numerical Stabilisation of Recovered Dark-Field Images

191 DF images are intrinsically noisy<sup>31,32</sup> in the sense that the diffuse scattering which underpins them is due  
 192 to extremely small unresolved spatially-random features within the sample. This leads to finely-fluctuating  
 193 unresolved speckle variations over individual pixels. By spatially averaging these high-frequency variations  
 194 across pixels, the DF signal is obtained. Gureyev *et al.*<sup>32</sup> developed a model based on the assumption of a  
 195 single-material sample for which the projected linear attenuation coefficient,  $\mu_p(\mathbf{r})$ , is a composite of a rapidly  
 196 varying component  $\mu_{\text{fast,p}}(\mathbf{r})$ , and a slowly-varying component  $\mu_{\text{slow,p}}(\mathbf{r})$ :

$$\mu_p(\mathbf{r}) = \mu_{\text{fast,p}}(\mathbf{r}) + \mu_{\text{slow,p}}(\mathbf{r}). \quad (19)$$

197 Here,  $\mu_{\text{slow,p}}(\mathbf{r})$  results from density variations over length scales larger than the pixel size, which hence can be  
 198 resolved in a typical phase-contrast image. Conversely,  $\mu_{\text{fast,p}}(\mathbf{r})$  is associated with unresolved microstructure in  
 199 the sample, which fluctuates rapidly throughout the sample, and hence across one detector pixel. The spatially-  
 200 averaged fast-varying component of the projected linear attenuation coefficient,  $\overline{\mu_{\text{fast,p}}(\mathbf{r})}$ , is connected to the  
 201 effective DF signal by:<sup>32</sup>

$$D_{\text{eff}}(\mathbf{r}; \Delta) = \frac{\delta}{\beta k} \overline{|\mu_{\text{fast,p}}(\mathbf{r})|^2}. \quad (20)$$

202 Here, the overline denotes spatial averaging over a single detector pixel. Since the above expression is obtained  
 203 via a spatial average of an intrinsically rapidly-varying and often-spatially-random quantity, the effective DF  
 204 signal is typically inherently noisy.

205 This ‘‘intrinsic noise’’ is closely related to the evident numerical division-by-zero instability in Eqn. (18). To  
 206 deal with this instability, we propose two alternative approaches to numerically stabilise this expression. Each  
 207 is considered in turn, below.

208 Method i) **Tikhonov Regularisation**: This is a well known mathematical technique<sup>60,61,63</sup> and can easily be  
 209 implemented by making the replacement, for any numerator and denominator  $A(\mathbf{r})$  and  $B(\mathbf{r})$ , of:

$$\frac{A(\mathbf{r})}{B(\mathbf{r})} \rightarrow \frac{A(\mathbf{r})B(\mathbf{r})}{[B(\mathbf{r})]^2 + \epsilon}. \quad (21)$$

212 Here,  $\epsilon$  is a positive regularisation parameter.

213 Method ii) **Weighted-Determinants**: This method utilises the determinant of the system of linear equations,  
 214 Eqn. (14). Moreover, the determinant is used as a weighting factor for the appropriate pairs of mask positions,  
 215  $a$  and  $b$ . The proposed method can be thought of as a type of the “weighted-mean”<sup>62</sup> approach often used in  
 216 the practice of statistics. The determinant of the system of linear equations is:

$$\text{Det}_{a,b}(\mathbf{r}) = \frac{\nabla_{\perp}^2 I_{Rb}(\mathbf{r})}{I_{Rb}(\mathbf{r})} - \frac{\nabla_{\perp}^2 I_{Ra}(\mathbf{r})}{I_{Ra}(\mathbf{r})}. \quad (22)$$

217 The determinant of a system of linear equations characterizes the stability of the solution. A system of linear  
 218 equations has a unique and stable solution if the determinant is nonzero. Therefore, as the determinant ap-  
 219 proaches zero, the solution becomes unstable. The determinant of Eqn. (14) is an array equal to the size of  
 220 the input projection images, and its elements will give a pixel-wise measure of how much to “trust” the cor-  
 221 responding element in the DF image. Then, given  $N$  different mask positions, we can calculate  $[N(N-1)/2]$   
 222 effective DF projection images, for each distinct pair of mask positions. The determinant of the appropriate  
 223 system of linear equations can then be calculated using Eqn. (22). The effective DF projection images can sub-  
 224 sequently be weighted by their appropriate squared determinant, summed, and normalised to give what we term  
 225 the “Weighted Determinant” effective DF projection image,  $\text{WD}[D_{\text{eff}}(\mathbf{r}; \Delta)]$ . To demonstrate this approach, we  
 226 present the weighted-determinant expression for three transverse positions of the mask,  $N = 3$ , however this can  
 227 be easily extended to a larger number of mask positions:

$$\text{WD}[D_{\text{eff}}(\mathbf{r}; \Delta)] = \frac{|\text{Det}_{1,2}(\mathbf{r})|^2 D_{\text{eff}}^{1,2}(\mathbf{r}) + |\text{Det}_{2,3}(\mathbf{r})|^2 D_{\text{eff}}^{2,3}(\mathbf{r}) + |\text{Det}_{1,3}(\mathbf{r})|^2 D_{\text{eff}}^{1,3}(\mathbf{r})}{|\text{Det}_{1,2}(\mathbf{r})|^2 + |\text{Det}_{2,3}(\mathbf{r})|^2 + |\text{Det}_{1,3}(\mathbf{r})|^2}. \quad (23)$$

### 228 3. EXPERIMENTAL DATA / PROCEDURE

229 The experimental X-ray data analyzed throughout the presented work was collected at the Imaging and Med-  
 230 ical Beamline (IMBL) at the Australian Synchrotron in Melbourne. This set of SBXI data was collected in  
 231 hutch 3B, which is often used for large-sample X-ray imaging and computed tomography, due to its large X-ray  
 232 beam-size. A Ruby detector<sup>64</sup> was used, which has a single pco.edge sensor and a lens-coupled scintillator. The  
 233 detector’s pixelation is  $2560 \times 2160$ , with an effective pixel size of  $12.5\mu\text{m}$ . The distance between the source  
 234 and beam entrance window for hutch 3B,  $smd$ , was  $135.8\text{m}$ , the distance between the mask and sample,  $msd$ ,  
 235 was  $1.019\text{m}$ , and the propagation distance,  $sdd = \Delta$ , between the sample and detector, was  $2.000\text{m}$ . The  
 236 speckle-generating mask had a typical grain size of  $30\text{--}45\mu\text{m}$ . The position of the mask was transversely shifted,  
 237 in the direction perpendicular to the beam, to acquire a total of six different sets of raw intensity projection data.  
 238

239 The sample investigated throughout was a wood sample, as shown in Fig. 1. This sample has three differ-  
 240 ent wood types,  $i)$  -  $iii)$ , mounted onto a metal cylindrical disk. The exact wood type of these samples was  
 241 unknown, however, key characteristics can be observed from Fig. 1.  
 242

243 SBXI was carried out on the wood sample with a monochromatic X-ray beam of energy  $30\text{keV}$ . Raw inten-  
 244 sity projection data were collected, namely three data sets: sample projections, mask-reference projections, and  
 245 dark-current projections. Sample projections included intensity variations arising from phase and attenuation  
 246 differences introduced by both the sample and specified mask, whereas the reference-speckle projections showed  
 247 just the image of the mask. The dark-current projection images were collected in the absence of X-rays, used  
 248 to correct for the detector. The acquired projection images were then processed within a Python3 script to  
 249 calculate the attenuation, projected thickness, and DF images.  
 250

251 The projected thickness, and hence attenuation, of the wood sample was calculated using Eqn. (18) from Pavlov  
 252 *et al.*,<sup>58</sup> with  $\gamma = \delta_{\text{wood}}/\beta_{\text{wood}} = 2990$ , assuming a generic composition of wood. The phase-object approximation  
 253 for the effective DF image was then calculated using a Tikhonov-Regularised weighted-determinant variant of  
 254 Eqn. (7), that is, the two methods in conjunction, from Pavlov,<sup>52</sup> or equivalently,

$$D_{\text{eff, Phase}}(\mathbf{r}; \Delta) = \frac{G_2(\mathbf{r})}{\Delta}, \quad (24)$$

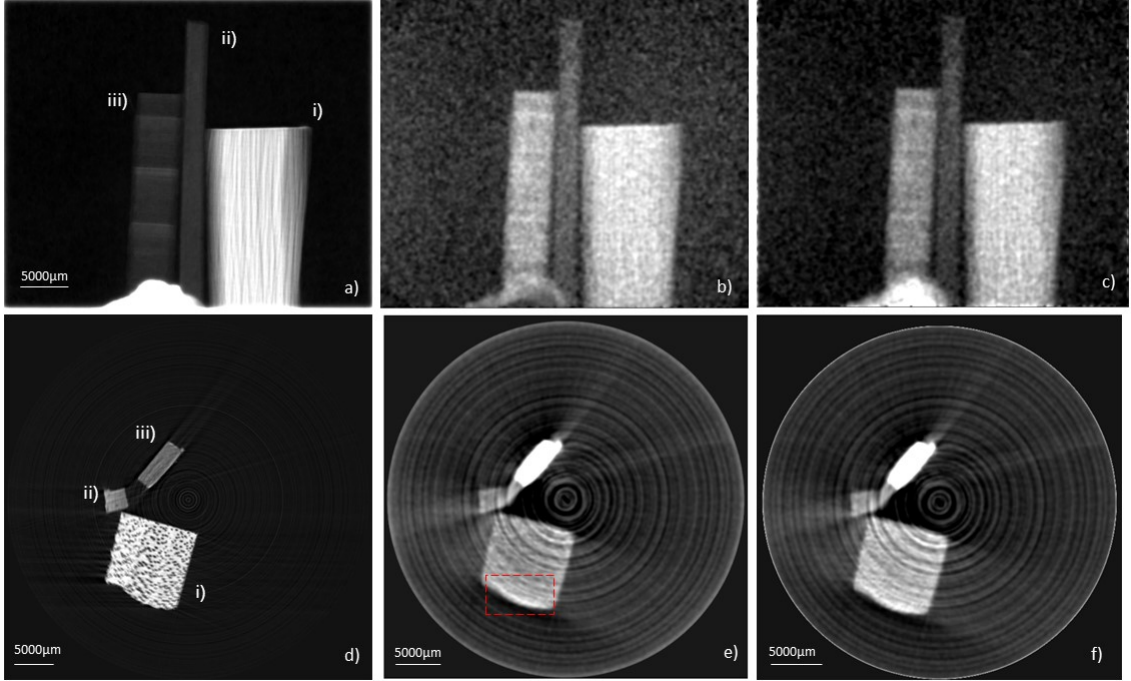


Figure 2. *Top row: Projection images, in the direction of the optical axis,  $z$ , of (a) projected-thickness, (b) effective dark-field signal generated using a phase-object approximation, and (c) attenuating-object approximation of the wood sample. Bottom row: Computed-Tomography (CT) reconstructions of (d) attenuation coefficient,  $\beta(\mathbf{r}')$ , (e) phase-object approximation for the dark-field, and (f) attenuating-object approximation for the dark-field. Wood labelling, i) – iii), refers to that in Fig. 1. All of the dark-field images, b), c), e), and f) have been post-processed with a 5 pixel standard deviation Gaussian filter*

255 as derived in this paper. From there, the attenuating-object approximation of the DF image was calculated  
 256 using, once again, a Tikhonov-regularised weighted-determinant form of Eqn. (18). As we had SBXI data for  
 257 six different well-resolved reference speckle-fields,  $N = 6$  in Eqn. (23), these were all utilized to calculate the  
 258 effective DF. All of the speckle-fields were included to maximise the DF signal quality and robustness to noise,  
 259 following Pavlov *et al.*<sup>52</sup>  
 260

#### 261 4. DISCUSSION / ANALYSIS

262 We have experimentally implemented the phase-object approximation to MIST<sup>52</sup> and then extended this to con-  
 263 sider a monomorphous attenuating object, by utilizing the already-presented multimodal X-ray Fokker-Planck  
 264 based speckle tracking approach.<sup>31</sup> Figures 2b and 2c demonstrate how the proposed extension of MIST<sup>52</sup> to  
 265 consider an attenuating-object, rather than a phase-object, more accurately models objects that attenuate the  
 266 X-ray beam significantly. An example of this is the feature at the bottom centre of Fig. 2b and 2c, namely Blu  
 267 Tack, which has strong attenuating and small-angle scattering characteristics. In the phase-object approximation  
 268 (see Fig. 2b), the effective DF is significantly suppressed in inner regions of the wood samples due to strong X-ray  
 269 attenuation. However, this effective DF is corrected in the attenuating-object approximation (see Fig. 2c) as the  
 270 object attenuation-term,  $I_{ob}(\mathbf{r})$ , has been considered.

271  
 272 The effective DF projection images have been numerically stabilised using the “Weighted-Determinant” ap-  
 273 proach, as well as Tikhonov regularisation, as given by Eqs. (21) and (23). We utilized the entirety of the  
 274 data set available, that is six transverse mask positions,  $N = 6$ , to maximize the signal-to-noise ratio in the  
 275 extracted DF signal. However, fewer mask positions were also investigated using the same approach, and the



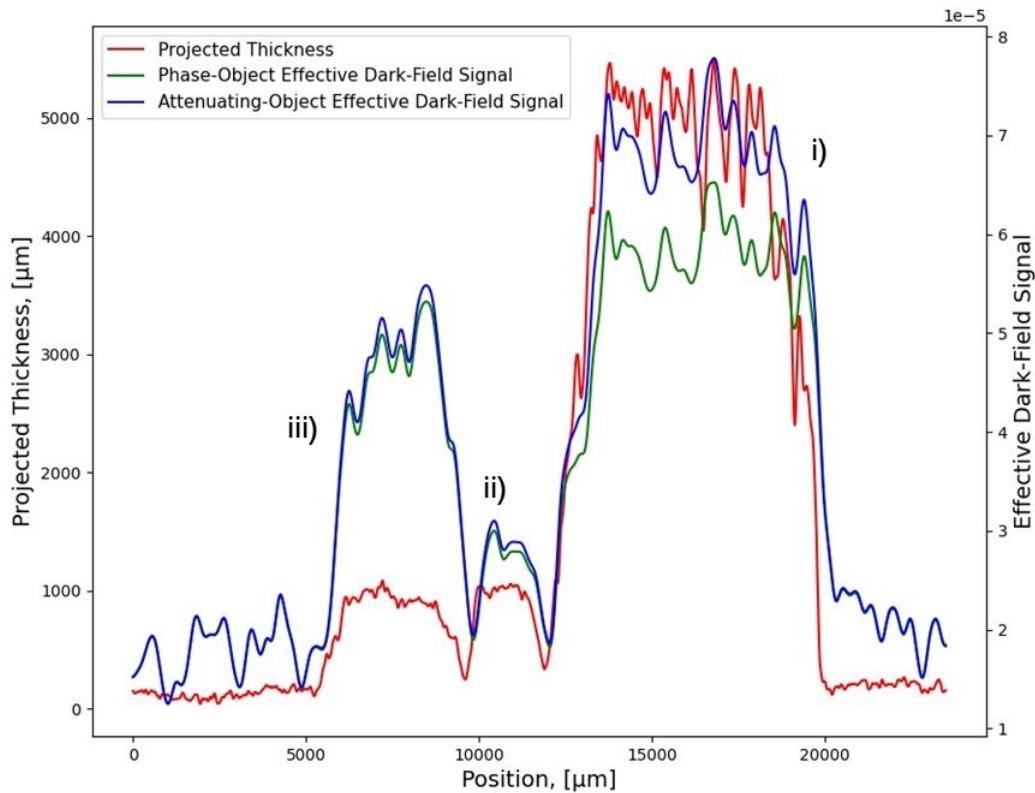


Figure 3. Line profiles across taken across each of the wood samples in the projection images of (red) projected thickness, (green) phase object approximation dark-field image, and (blue) attenuating object approximation dark-field image. Wood labelling, *i* – *iii*), refers to that in Fig. 1.

276 results agreed with that of Pavlov *et al.*,<sup>52,53</sup> demonstrating that two mask positions are sufficient to extract a  
 277 measurable DF signal. The quality of the reconstructed DF signal was clearly improved using the Tikhonov-  
 278 regularised weighted-determinant method. This optimisation of effective DF projection images (Figs. 2b and 2c)  
 279 then allowed standard CT algorithms to be used to reconstruct axial slices (Figs. 2e and 2f). Here, XTRACT<sup>65</sup>  
 280 software was used to implement a filtered-backprojection CT reconstruction algorithm, with a Hamming fil-  
 281 ter being used for noise suppression.<sup>66</sup> The weighted-determinant variant of numerical stabilisation was less  
 282 computationally expensive, giving a reduction of a factor of 100 in computation time, compared to other tri-  
 283 alled techniques, for example having a pixel-wise matrix inversion to obtain the solution in a least-squares<sup>67</sup> sense.

284  
 285 Figures 2 and 3 demonstrate the differing structural information obtained in bright-field, standard PCI, and  
 286 DF imaging, and also how the presented monomorphous attenuating-object description compares to the previ-  
 287 ously published<sup>52</sup> phase-object approach. The projected thickness, Fig. 2a, displays the fibre-like features in the  
 288 wood: these run horizontally in sample *iii*) and vertically in sample *i*). Such features are also resolvable in the  
 289 DF images, Fig. 2b and 2c, alongside further variations in structural characteristics. It is interesting to note that  
 290 while sample *iii*) has the weakest contrast of the three samples in the attenuation coefficient image in Fig. 2d,  
 291 this sample has the strongest contrast of the three samples in the DF images shown in Fig. 2e and Fig. 2f. The  
 292 power of DF imaging is accentuated in Fig. 2, particularly the complementary information for samples *ii*) and  
 293 *iii*). Moreover, although the projected thickness is equal for these two samples, sample *iii*) has a factor of 2  
 294 greater effective DF signal than *ii*). These characteristics are also shown in the CT reconstructions. Indeed,  
 295 there is further structural information about the wood sample that is revealed in the CT reconstructions and not  
 296 seen in the projection images. For example, as previously mentioned, in the axial slice shown in Fig. 2, sample

297 *ii*) has the largest effective DF signal, yet the lowest attenuation coefficient,  $\beta(\mathbf{r}')$ . An unseen structural feature  
298 also appears in the DF-CT reconstruction of wood sample *i*) that is not in the PCI-CT, marked in red.

299  
300 Equation (18) was used to calculate the effective DF signal, shown in Fig. 2, which was derived under the  
301 assumption that the SAXS fans emanating from the exit-surface of the sample are rotationally symmetric. How-  
302 ever, the sample studied within, wood, typically has anisotropic scattering structures, and thus one might think  
303 that the key assumption (i.e., rotational symmetry of the position-dependent SAXS fans that underpin the DF  
304 signal) is violated. However, we see in Figs. 2 and 3, that the isotropic attenuating-object approximation, which  
305 improves upon the isotropic phase-object approximation, extracts a first approximation (i.e., rotationally sym-  
306 metric) of the dark-field signal that well represents the wood sample. Stated differently, the locally-elliptical  
307 position-dependent SAXS fans may be reasonably approximated as rotationally symmetric, to give lowest-order  
308 position-dependent information regarding this scattering channel. This suggests that the formalism presented  
309 in our paper is capable of providing directionally-averaged DF information, for objects that may violate the  
310 underlying assumptions of rotationally-symmetric position-dependent SAXS fans.

311  
312 Equation (18) is also, in theory, restricted to monomorphous objects. This arises from the definition of  $\gamma$   
313 used for phase-contrast signal extraction, which is used to calculate  $I_{\text{ob}}(\mathbf{r})$ , which is then required to calculate  
314 the DF of an attenuating object. This single-material restriction can be extended to a two-component sample by  
315 taking the difference between the real and imaginary components of refractive index for each material.<sup>68</sup> This  
316 representation of  $\gamma$  results in correctly phase-retrieved interfaces between the two materials. In multi-material  
317 samples, if  $\gamma$  for specific interfaces between two materials deviates too far from the inputted value then the phase-  
318 contrast signal will be either over- or under-compensated.<sup>69</sup> However, Gureyev *et al.*<sup>70</sup> report that an incorrect  
319 choice of  $\gamma$  does not affect the extracted  $\beta$  far away from the interface. Hence, this underlying monomorphous  
320 restriction would only be detrimental to the reconstructed DF if the sample had many composite materials that  
321 had greatly differing attenuation and refraction properties. In such cases, there would be a large range of  $\gamma$  values  
322 for specific interfaces within the sample, hence, edge-effects would exist in both the PCI and DF reconstructions.  
323 The described case is unlikely in applications, and this is further supported by wide adoption of Paganin's single-  
324 material TIE-Hom phase-retrieval algorithm<sup>7</sup> in various disciplines. We refer the reader to the introduction in  
325 Paganin *et al.*<sup>71</sup> where the utility domain of the single-material approach is discussed in-depth. Many objects  
326 can be viewed as being locally composed of a single material, in three dimensions, even though such materials  
327 may not contain a single-material in projections. It is possible to apply a fast localized 3D reconstruction for  
328 such isolated single-material regions.<sup>72</sup> Also, in biomedical applications, the single-material assumption is still  
329 appropriate at high X-ray energies where biomedical samples, for example soft-tissues, can be considered as a  
330 single material,<sup>73</sup> that is, a cloud of electrons.

331  
332 DF imaging provides complementary information to both conventional attenuation-based imaging, which is  
333 currently employed in clinics, and PCI. SBXI is experimentally simple and requires fewer sample exposures,  
334 than alternative X-ray imaging techniques, that extract multi-modal signals. Within, we have demonstrated  
335 that an intrinsic speckle-tracking approach to SBXI allows both projection and tomographic reconstruction of  
336 phase-contrast and DF signals for a monomorphous attenuating object, which when considered in parallel provide  
337 complementary information. In a clinical/biomedical setting, the additional information provided by DF tomog-  
338 raphy could prove to be highly useful in diagnostic studies. A recent publication, Willer *et al.*,<sup>74</sup> demonstrates  
339 X-ray DF imaging in a clinical application, namely chest imaging. Willer *et al.* used a grating-interferometry  
340 X-ray imaging technique, which requires a precisely-aligned experimental set-up, but also enables the use of large  
341 pixels for large-area imaging. SBXI utilises a less-demanding set-up, but must directly resolve changes to the  
342 speckle pattern, hence is best suited for smaller samples.

## 343 5. CONCLUSION

344 We have developed a monomorphous attenuating-object variant of the phase-object MIST X-ray speckle-tracking  
345 method proposed in 2020 by Pavlov *et al.*<sup>52</sup> Our method has been demonstrated on experimental data to achieve  
346 speckle-based X-ray DF tomography. A numerical stabilisation approach, namely the "Weighted Determinant"  
347 method, together with Tikhonov Regularisation, was used to stabilise the intrinsic noise of DF images. These

348 reconstructions are based on six sets of images acquired at different transverse positions of the speckle mask.  
349 However, reconstructions based on two images, as reported also by Pavlov *et al.*,<sup>52</sup> give comparable reconstruc-  
350 tions, albeit with higher noise on account of the smaller number of measurements that are required.

## 351 DISCLOSURES

352 All authors within the presented manuscript report no relevant conflicts of interest or financial interests with  
353 respect to this work.

## 354 ACKNOWLEDGMENTS

355 This research was undertaken on the Imaging and Medical beamline (proposal AS193/IMBL/15230) at the  
356 Australian Synchrotron, part of ANSTO. The authors also acknowledge Emmanuel Brun for providing the  
357 speckle generating membrane used for image acquisition, and the University of Canterbury for awarding a  
358 Doctoral Scholarship to S. J. Alloo. This paper is based on a published SPIE conference proceeding paper.<sup>75</sup>

## 359 REFERENCES

- 360 [1] Röntgen, W. C. “Über eine neue Art von Strahlen”, *Sitzungsberichte der Physikalisch-medizinischen*  
361 *Gesellschaft zu Würzburg* Vol. 28, 132–141 (1895).
- 362 [2] Pelliccia, D., Kitchen, M. J. & Morgan, K. S. “Handbook of X-ray Imaging: Physics and Technology, ch. 49,  
363 Theory of X-ray Phase-Contrast Imaging”, *CRC Press* (2018).
- 364 [3] Snigirev, A., Snigireva, I., Kohn, V., Kuznetsov, S., & Schelokov, I. “On the possibilities of X-ray phase  
365 contrast microimaging by coherent high-energy synchrotron radiation”, *Rev. Sci. Instrum.* Vol. 66, 5486–5492  
366 (1995).
- 367 [4] Wilkins, S. W., Gureyev, T. E., Gao, D., Pogany, A., & Stevenson, A. W. “Phase-contrast imaging using  
368 polychromatic hard X-rays”, *Nature* Vol. 384, 335–338 (1996).
- 369 [5] Nugent, K. A., Gureyev, T. E., Cookson, D. F., Paganin, D., & Barnea, Z. “Quantitative phase imaging  
370 using hard X-rays”, *Phys. Rev. Lett.* Vol. 77, 2961-2964 (1996).
- 371 [6] Cloetens, P., Barrett, R., Baruchel, J., Guigay, J.-P. & Schlenker, M. “Phase objects in synchrotron radiation  
372 hard x-ray imaging”, *J. Phys. D: Appl. Phys.* Vol. 29, 133-146 (1996).
- 373 [7] Paganin, D., Mayo, S. C., Gureyev, T. E., Miller, P. R., & Wilkins, S. W. “Simultaneous phase and amplitude  
374 extraction from a single defocused image of a homogeneous object”, *J. Microsc.* Vol. 206, 33-40 (2002).
- 375 [8] Teague, M. R. “Deterministic phase retrieval: a Green’s function solution”, *J. Opt. Soc. Am. A* Vol. 73,  
376 1434-1441 (1983).
- 377 [9] David, C., Nöhammer, B., Solak, H. H., & Ziegler, E. “Differential x-ray phase contrast imaging using a  
378 shearing interferometer”, *Appl. Phys. Lett.* Vol. 81, 3287-3289 (2002).
- 379 [10] Momose, A., Kawamoto, S., Koyama, I., Hamaishi, Y., Takai, K. & Suzuki, Y. “Demonstration of X-ray  
380 Talbot interferometry”, *Jpn J. Appl. Phys.* Vol. 42, L866-L868 (2003).
- 381 [11] Weitkamp, T., Nöhammer, B., Diaz, A., David, C., & Ziegler, E. “X-ray wavefront analysis and optics  
382 characterization with a grating interferometer”, *Appl. Phys. Lett.* Vol. 86, 054101 (2005).
- 383 [12] Weitkamp, T., Diaz, A., David, C., Pfeiffer, F., Stampanoni, M., Cloetens, P. & Ziegler, E. “X-ray phase  
384 imaging with a grating interferometer”, *Opt. Express* Vol. 13, 6295-6304 (2005).
- 385 [13] Pfeiffer, F., Weitkamp, T., Bunk, O. & David, C. “Phase retrieval and differential phase-contrast imaging  
386 with low-brilliance X-ray sources”, *Nat. Phys.* Vol. 2, 258-261 (2006).
- 387 [14] Momose, A., Yashiro, W., Takeda, Y., Suzuki, Y. & Hattori, T. “Phase tomography by X-ray Talbot  
388 interferometry for biological Imaging”, *Jpn J. Appl. Phys.* Vol. 45, 5254-5262 (2006).
- 389 [15] Takeda, Y., Yashiro, W., Suzuki, Y., Aoki, S., Hattori, T. & Momose, A. “X-Ray phase imaging with single  
390 phase grating”, *Jpn J. Appl. Phys.* Vol. 46, L89-L91 (2007).
- 391 [16] Bonse, U. & Hart, M. “An x-ray interferometer”, *Appl. Phys. Lett.* Vol. 6, 155–156 (1965).
- 392 [17] Momose, A. “Demonstration of phase-contrast X-ray computed tomography using an X-ray interferometer”,  
393 *Nucl. Instrum. Methods Phys. Res. A* Vol. 352, 622-628 (1995).

- 394 [18] Wen, H., Gomella, A. G., Patel, A., Wolfe, D. E., Lynch, S. K., Xiao, X., & Morgan, N. “Boosting phase  
395 contrast with a grating Bonse–Hart interferometer of 200 nanometre grating period”, *Philos. Trans. A. Math.*  
396 *Phys. Eng. Sci.* Vol. 372, 20130028 (2010).
- 397 [19] Olivo, A. & Speller, R. “A coded-aperture technique allowing x-ray phase contrast imaging with conventional  
398 sources”, *Appl. Phys. Lett.* Vol. 074106, 074106 (2007).
- 399 [20] Olivo, A., Arfelli, F., Cantatore, G., Longo, R., Menk, R. H., Pani, S., Prest, M., Poropat, P., Rigon, L.,  
400 Tromba, G., Vallazza, E., & Castelli, E. “An innovative digital imaging set-up allowing a low-dose approach  
401 to phase contrast applications in the medical field”, *Med. Phys.* Vol. 28, 1610-1619 (2001).
- 402 [21] Goetz, K., Kalashnikov, M. P., Mikhailov, Y. A., Sklizkov, G. V., Fedotov, S. I., Foerster, E., & Zaumseil,  
403 P. “Measurement of parameters of shell targets for laser fusion with the use of X-ray schlieren technique”,  
404 *Sov. J. Quant. Electron.* Vol. 9, 607–610 (1979).
- 405 [22] Somenkov, V. A., Tklich, A. K. & Shil’shtein, S. Sh. “Refraction contrast in x-ray introscopy”, *Sov. Phys.*  
406 *Tech. Phys.* Vol. 36, 1309-1311 (1991).
- 407 [23] Ingal, V. N., & Beliaevskaya, E. A. “X-ray plane-wave topography observation of the phase contrast from  
408 a noncrystalline object”, *J. Phys. D: Appl. Phys.* Vol. 28, 2314–2317 (1995).
- 409 [24] Davis, T. J., Gao, D., Gureyev, T. E., Stevenson, A. W. & Wilkins, S. W. “Phase-contrast imaging of  
410 weakly absorbing materials using hard X-rays”, *Nature* Vol. 373, 595-598 (1995).
- 411 [25] Wernick, M. N., Wirjadi, O., Chapman, D., Zhong, Z., Galatsanos, N. P., Yang, Y., Brankov, J. G., Oltulu,  
412 O., Anastasio, M. A., & Muehleman, C. “Multiple-image radiography”, *Phys. Med. Biol.* Vol. 48, 3875–3895  
413 (2003).
- 414 [26] Berujon, S., Ziegler, E., Cerbino, R., & Peverini, L. “Two-Dimensional X-Ray Beam Phase Sensing”, *Phys.*  
415 *Rev. Lett.* Vol. 108, 158102 (2012).
- 416 [27] Morgan, K. S., Paganin, D. M., & Siu, K. K. W. “X-ray phase imaging with a paper analyser”, *Appl. Phys.*  
417 *Lett.* Vol. 100, 124102 (2012).
- 418 [28] Zdora, M.-C. “State of the art of X-ray speckle-based phase-contrast and dark-field imaging”, *J. Imaging*,  
419 Vol. 4, 60 (2018).
- 420 [29] Kratky, O. and Glatter, O. “Small Angle X-ray Scattering”, *Academic Press* (1982).
- 421 [30] Sabatier, P. C. “Past and future of inverse problems”, *J. Math. Phys.* Vol. 41, 4082-4124 (2000).
- 422 [31] Paganin, D. M., & Morgan, K. S. “X-ray Fokker-Planck equation for paraxial imaging”, *Sci. Rep.* Vol. 9,  
423 17537 (2019).
- 424 [32] Gureyev, T. E., Paganin, D. M., Arhatari, B., Taba, S. T., Lewis, S., Brennan, P. C., & Quiney, H. M.  
425 “Dark-field signal extraction in propagation-based phase-contrast imaging”, *Phys. Med. Biol.* Vol. 65, 215029  
426 (2020).
- 427 [33] Pfeiffer, F., Bech, M., Bunk, O., Kraft, P., Eikenberry, E. F., Brönnimann, C., Grünzweig, C., & David, C.  
428 “Hard-X-ray dark-field imaging using a grating interferometer”, *Nature. Mat.* Vol. 7, 2, 134-137 (2008).
- 429 [34] Velroyen, A., Yaroshenko, A., Hahna, D., Fehringer, A., Tapfer, A., Müller, M., Noël, P. B., Pauwels, B.,  
430 Sasov, A., Yildirim, A. Ö., Eickelberg, E., Hellbach, K., Auweter, S. D., Meinel, F. G., Reiser, M. F., Bech,  
431 M., & Pfeiffer, F. “Grating-based X-ray dark-field computer tomography of living mice”, *E. Bio. Medicine*  
432 Vol. 2, 1500–1506 (2015).
- 433 [35] Pfeiffer, F., Bech, M., Bunk, O., Donath, T., Henrich, B., Kraft, P., & David, C. “X-ray dark-field and  
434 phase-contrast imaging using a grating interferometer”, *J. Appl. Phys.* Vol. 105, 102006 (2009).
- 435 [36] Yaroshenko, A., Hellbach, K., Bech, M., Grandl, S., Reiser, M. F., Pfeiffer, F., & Meinel, F. G. “Grating-  
436 based X-ray dark-field imaging: a new paradigm in radiography”, *Curr. Radiol. Rep.* Vol 2, 57 (2014).
- 437 [37] Endrizzi, M., Murat, B. I. S., Fromme, P., & Olivo, A. “Edge-illumination X-ray dark-field imaging for  
438 visualising defects in composite structures”, *Compos. Struct.* Vol. 145, 895-899 (2015).
- 439 [38] Matsunaga, N., Yano, K., Endrizzi, M., & Olivo, A. “Detection of individual sub-pixel features in edge-  
440 illumination x-ray phase contrast imaging by means of the dark-field channel”, *J. Phys. D: Appl. Phys.* Vol.  
441 53, 095401 (2019).
- 442 [39] Pagot, E., Cloetens, P., Fiedler, S., Bravin, A., Coan, P., Baruchel, J., Härtwig, J., & Thomlinson, W. “A  
443 method to extract quantitative information in analyzer-based x-ray phase contrast imaging”, *Appl. Phys. Lett.*  
444 Vol. 82, 3421-3423 (2003)

- 445 [40] Majidi, K., Brankov, J. G., & Wernick, M. N. “Sampling Strategies in Multiple-Image Radiography”, *2008*  
446 *5th IEEE International Symposium on Biomedical Imaging: From Nano to Macro*, 688-691 (2008).
- 447 [41] Ando, M., Sunaguchi, N., Shima, D., Pan, A., Yuasa, T., Mori, K., Suzuki, Y., Jin, G., Kim, J., Lim,  
448 J., Seo, S., Ichihara, S., Ohura, N., & Gupta, R. “Dark-Field Imaging: Recent developments and potential  
449 clinical applications”, *Phys. Medica* Vol. 32, 1801-1812 (2016).
- 450 [42] Ando, M., Nakao, Y., Jin, G., Sugiyama, H., Sunaguchi, N., Sung, Y., Suzuki, Y., Sun, Y., Tanimoto, M.,  
451 Kawashima, K. & Yuasa, T. “Improving contrast and spatial resolution in crystal analyser-based X-ray dark-  
452 field imaging: Theoretical considerations and experimental demonstration”, *Med. Phys.* Vol. 47, 5505-5513  
453 (2020).
- 454 [43] Bennett, E. E., Kopace, R., Stein, A. F., & Wen, H. “A grating-based single-shot x-ray phase contrast and  
455 diffraction method for in vivo imaging”, *Med. Phys.* Vol. 37, 6047-6054 (2010).
- 456 [44] Morgan, K. S., Paganin, D. M. & Siu, K. K. W. “Quantitative single-exposure x-ray phase contrast imaging  
457 using a single attenuation grid”, *Opt. Express* Vol. 19, 19781-19789 (2011).
- 458 [45] Kitchen, M. J., Pavlov, K. M., Hooper, S. B., Vine, D. J., Siu, K., Wallace, M. J., Siew, M. L. L., Yagi, N.,  
459 Uesugi, K., & Lewis, R. A. “Simultaneous acquisition of dual analyser-based phase contrast X-ray images for  
460 small animal imaging”, *Eur. J. Radiol.* Vol. 68, S49-S53 (2008).
- 461 [46] Kitchen, M. J., Paganin, D. M., Uesugi, K., Allison, B. J., Lewis, R. A., Hooper, S. B., & Pavlov, K. M.  
462 “X-ray phase, absorption and scatter retrieval using two or more phase contrast images”, *Opt. Express* Vol.  
463 18, 19994-20012 (2010).
- 464 [47] Kitchen, M. J., Paganin, D. M., Uesugi, K., Allison, B. J., Lewis, R. A., Hooper, S. B., & Pavlov, K. M.  
465 “Phase contrast image segmentation using a Laue analyser crystal”, *Phys. Med. Biol.* Vol. 56, 515-534 (2011).
- 466 [48] Berujon, S., Wang, H., & Sawhney, K., “X-ray multimodal imaging using a random phase object,” *Phys.*  
467 *Rev. A*, Vol. 86, 6, 063813 (2012).
- 468 [49] Zdora, M.-C., Thibault, P., Zhou, T., Koch, F. J., Romell, J., Sala, S., Last, A., Rau, C., & Zanette, I.  
469 “X-ray phase-contrast imaging and metrology through unified modulated pattern analysis”, *Phys. Rev. Lett.*  
470 Vol. 118, 203903 (2017)
- 471 [50] Zanette, I., Zhou, T., Burvall, A., Lundström, U., Larsson, D. H., Zdora, M., Thibault, P., Pfeiffer, F.,  
472 & Hertz, H. M. “Speckle-based x-ray phase-contrast and dark-field imaging with a laboratory source”, *Phys.*  
473 *Rev. Lett.* Vol. 112, 253903 (2014).
- 474 [51] Berujon, S., & Ziegler, E. “X-ray multimodal tomography using speckle-vector tracking”, *Phys. Rev. Appl.*,  
475 Vol. 5, 044014 (2016).
- 476 [52] Pavlov, K. M., Paganin, D. M., Li, H., Berujon, S., Rougé-Labriet, H. T., & Brun, E. “X-ray multi-modal  
477 intrinsic-speckle-tracking”, *J. Opt.* Vol. 22, 125604 (2020).
- 478 [53] Pavlov, K. M., Paganin, D. M., Morgan, K. S., Li, H., Berujon, S., Quénot, L., & Brun, E. “Directional  
479 dark-field implicit x-ray speckle tracking using an anisotropic-diffusion Fokker-Planck equation”, *Phys. Rev.*  
480 *A*, Vol. 105, 5, 053505 (2021).
- 481 [54] Morgan, K. S., & Paganin, D. M. “Applying the Fokker-Planck equation to grating-based x-ray phase and  
482 dark-field imaging”, *Sci. Rep.* Vol. 9, 17465 (2019).
- 483 [55] Risken, H. “The Fokker-Planck Equation: Methods of Solution and Applications: 2nd edn”, *Springer*  
484 (1989).
- 485 [56] Paganin, D. M., Labriet, H., Brun, E., & Berujon, S. “Single-image geometric-flow x-ray speckle tracking”,  
486 *Phys. Rev. A* Vol. 98, 053813 (2018).
- 487 [57] Willer, K., Fingerle, A.A., Gromann, L.B., De Marco, F., Herzen, J., Achterhold, K., Gleich, B., Muenzel,  
488 D., Scherer, K., Renz, M. & Renger, B. “X-ray dark-field imaging of the human lung – A feasibility study on  
489 a deceased body”, *PLoS One* Vol. 13, e0204565 (2018).
- 490 [58] Pavlov, K. M., Li, H. T., Paganin, D. M., Berujon, S., Rougé-Labriet, & Brun, E. “Single-shot x-ray  
491 speckle-based imaging of a single-material object”, *Phys. Rev. Appl.* Vol. 13, 054023 (2020).
- 492 [59] Paganin, D. M. “Coherent X-ray Optics”, *Oxford University Press* (2006).
- 493 [60] Tikhonov, A. N., & Arsenin, V. Y. “Solution of Ill-posed Problems”, *Winston & Sons* (1977).
- 494 [61] Fathi, E., & M. M., Shoja. “Deep Neural Networks for Natural Language Processing”, *Handbook of Statis-*  
495 *tics*, Vol. 38, Chapter 9, 229-316 (2018).

- 496 [62] Meier, P. "Variance of a weighted mean", *Biometrics*, Vol. 9, 1, 59-73 (1953).
- 497 [63] Murli, A., D'Amore, L., & De Simone, V. "The Wiener filter and regularisation methods for image restora-  
498 tion problems", *Proceedings 10th International Conference on Image Analysis and Processing, Venice, Italy*,  
499 394-399 (1999).
- 500 [64] Australian Synchrotron, ANSTO. "Preparation for imaging and computing tomography experiments".  
501 *IMBL*. Retrieved From: [http://archive.synchrotron.org.au/index.php?option=com\\_content&view=](http://archive.synchrotron.org.au/index.php?option=com_content&view=article&id=811&catid=31&Itemid=101)  
502 [article&id=811&catid=31&Itemid=101](http://archive.synchrotron.org.au/index.php?option=com_content&view=article&id=811&catid=31&Itemid=101) (2020).
- 503 [65] Gureyev, T. E., Nesterets, Y., Ternovski, D., Thompson, D., Wilkins, S. W., Stevenson, A. W., Sakellariou,  
504 A., & Taylor, J. A. "Toolbox for advanced X-ray image processing", *Proc. SPIE*, 8141, 81410B, Version 8.14.0.0  
505 (2011).
- 506 [66] Kak, A. C., & Slaney, M. "Principles of Computerized Tomographic Imaging", *IEEE Press* (1988).
- 507 [67] Press, W. H., Teukolsky, S. A., Vetterling, W. T., & Flannery, B. P. "Numerical Recipes in FORTRAN:  
508 The Art of Scientific Computing (2nd edn)", *Cambridge University Press* (1996).
- 509 [68] Gureyev, T. E., Stevenson, A. W., Paganin, D. M., Weitkamp, T., Snigirev, A., Snigireva, I., & Wilkins, S.  
510 W. "Quantitative analysis of two-component samples using in-line hard X-ray images", *J. Synchrotron Radiat.*  
511 Vol. 9, 3, 148-153 (2002).
- 512 [69] Beltran, M. A., Paganin, D. M., Uesugi, K., & Kitchen M. J. "2D and 3D X-ray phase retrieval of multi-  
513 material objects using a single defocus distance", *Opt. Express* Vol. 18, 6423-6436 (2010).
- 514 [70] Gureyev, T. E., Mohammadi, S., Nesterets, Y., Dullin, C., & Tromba, G. "Accuracy and precision of  
515 reconstruction of complex refractive index in near-field single-distance propagation-based phase-contrast to-  
516 mography", *J. Appl. Phys.* Vol. 114, 144906 (2013).
- 517 [71] Paganin, D. M., Favre-Nicolin, V., Mirone, A., Rack, A., Villanova, J., Olbinado, M.P., Fernandez, V., da  
518 Silva, J.C. and Pelliccia, D. "Boosting spatial resolution by incorporating periodic boundary conditions into  
519 single-distance hard-x-ray phase retrieval", *J. Opt.* Vol. 22, 115607 (2020).
- 520 [72] Thompson, D. A., Nesterets, Ya. I., Pavlov, K. M. & Gureyev, T.E. "Fast three-dimensional phase retrieval  
521 in propagation-based X-ray tomography", *J. Synchrotron Radiat.* Vol. 26, 3, 825-838 (2019).
- 522 [73] Wu, X., Liu, H., & Yan, A. "X-ray phase-attenuation duality and phase retrieval", *Opt. Lett.* Vol. 30, 4,  
523 379-381 (2005).
- 524 [74] Willer, K., Fingerle, A. A, Noichl, W., De Marco, F., Frank, M., Urban, T., Schick, R., Gustschin, A.,  
525 Gleich, B., Herzen, J., Koehler, T., Yaroshenko, A., Pralow, T., Zimmermann, G. S., Renger, B., Sauter,  
526 A. P., Pfeiffer, D., Makowski, M. R., Rummeny, E. J., Grenier, P. A., & Pfeiffer, F. "X-ray dark-field chest  
527 imaging for detection and quantification of emphysema in patients with chronic obstructive pulmonary disease:  
528 a diagnostic accuracy study", *The Lancet Digit. Health*, Vol. 3, 11, e733-e744 (2021).
- 529 [75] Alloo, S. J., Paganin, D. M., Morgan, K. S., Kitchen, M. J., Stevenson, A. W., Mayo, S. C., Li, H. T.,  
530 Kennedy, B., Maksimenko, A., Bowden, J., & Pavlov, K. M. "Speckle-Based X-Ray Dark-Field Tomography  
531 of an Attenuating Object", *Proc. SPIE* Vol. 11840, 118400G (2021).